Optical mode structure of the plasma waveguide

T. R. Clark* and H. M. Milchberg
Institute for Physical Science and Technology, University of Maryland, College Park, Maryland 20742
(Received 14 June 1999)

The quasibound modes of an evolving plasma waveguide were investigated by using variably delayed end-injected and side-injected probe pulses. The use of these different coupling geometries allowed the probing of the waveguide's optical modes during two temporal regimes: early-time plasma channel development, characterized by leaky optical confinement, and later channel hydrodynamic expansion characterized by stronger confinement. The wave equation was solved to determine the available quasiguided optical modes and their confinement for experimentally measured electron density profiles. The guided intensity patterns and spectra measured at the waveguide exit were successfully explained in terms of these mode solutions. The spectrum of broadband end-coupled probe pulses was found to be unaffected by the guiding process, mainly because those modes which survived to the waveguide exit were well-bound, and for strongly bound fields, the transverse mode profiles are wavelength independent. By contrast, side coupling to the quasibound modes of the plasma waveguide was seen to be highly mode and frequency selective.

PACS number(s): 42.25.Bs, 52.40.Nk, 52.50.Jm, 42.81.Wg

I. INTRODUCTION

The development of compact ultrashort pulse high intensity laser systems in recent years has made possible a new realm of laser-matter interaction [1]. In many experiments, laser-atom and laser-plasma interactions commonly take place in an intensity regime far beyond the applicability of perturbation theory. At even higher intensity ($>\sim 10^{18}$ W/cm^2), relativistic effects are now practically obtainable by many researchers [2]. In many applications, a long interaction zone between the intense laser pulse and the excited material is desirable, and optical guiding of the pulse will satisfy this requirement. The optical guiding of extremely intense pulses over many Rayleigh lengths in plasma has applications to coherent generation of short wavelength radiation [3,4], x-ray lasers [5], and laser-driven plasma accelerators [6].

Several schemes for the guiding of intense pulses have been demonstrated, where either a preformed plasma is used [7,8], or relativistic self-guiding takes place [9]. We have developed a method for producing a preformed plasma waveguide using the laser-induced breakdown along the line focus of an axicon lens [10]. In this scheme, the elongated, hot plasma formed during the breakdown expands radially, generating a shock wave on its periphery, and leaving an electron density minimum on axis. The resulting electron density profile can optically guide intense laser pulses, since the local refractive index increases where the electron density decreases. Using this method, we have guided pulses for up to 100 Rayleigh lengths [11] and at intensities as high as $\sim 10^{17}$ W/cm^2 [12].

In this paper, we explore the linear guiding properties of the plasma waveguide during its early rapid hydrodynamic evolution (<1 ns) and its later, slower evolution as it expands radially (<10 ns). Two different probing geometries were employed to study the optical mode confinement during these two temporal regimes. The subnanosecond regime was probed by transverse injection of the probe pulse through the wall of the channel [13], which we call side or tunnel coupling, while the later time evolution was probed through longitudinal injection of the probe pulse at the end of the waveguide, here called end coupling.

The onset of a density profile suitable for guiding is shown in Fig. 1, which shows a sequence of electron density profiles measured with picosecond resolution interferometry [10]. The 1 cm long plasma waveguide has been generated using a 350 mJ, 100 ps, 1064 nm pulse, focused by a 35° base angle axicon. The on-axis intensity in the line focus was $\sim 3\times 10^{13}$ W/cm^2. It is seen that early in time (<0.4 ns), the electron density has rapidly increased through a combination of field ionization and avalanche ionization. At longer times, a central depression in the density appears, and a shock front develops as the plasma expands into the neutral background

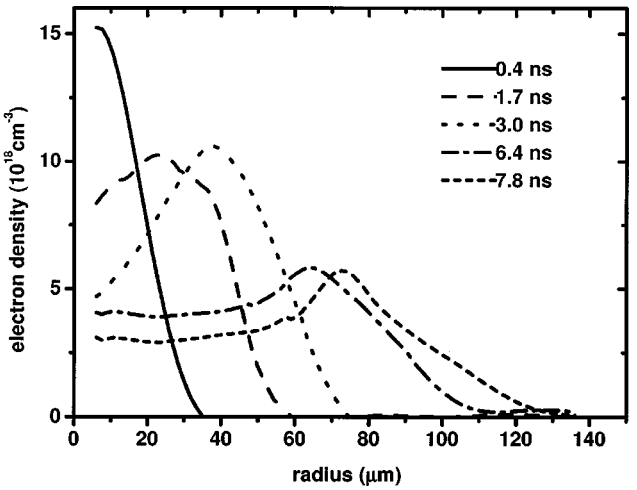

FIG. 1. Measured density profiles for a plasma created by a 350 mJ, 100 ps, 1064 nm pulse focused to a 1 cm line focus with on-axis intensity $\sim 3\times 10^{13}$ W/cm^2 in a 105/20 torr Ar/N_2O backfill gas target.

*Present address: Optical Sciences Division, Code 5650, Naval Research Laboratory, Washington, DC 20375.

gas. As the channel expands, the density depression widens and the central density drops. At all delays, the electron density drops to zero at sufficient radius.

II. OPTICAL MODES OF THE PLASMA WAVEGUIDE

The Fourier transformed wave equation for the electric field of a laser pulse propagating in a dielectric medium is

$$\nabla^2\tilde{E}+\frac{\omega^2}{c^2}n^2\tilde{E}=\nabla\left(-\frac{1}{n^2}\tilde{E}\cdot\nabla n^2\right), \tag{1}$$

where the refractive index $n=n(\vec{r},\omega)$ contains both the plasma and neutral medium contributions. The wave equation for the magnetic field has a similar form. We are interested in solutions which propagate along the plasma waveguide axis, taken to be along z. The right hand side of Eq. (1), called the polarization term, will in general have a z component, so that $\tilde{E}$ will also require a z component. This follows because $\tilde{E}$ is generally dependent on z. The condition for the polarization term to be negligible compared to the equation's left side is $E\Delta n^2/n^2L_t^2\ll\Delta E/L_t^2$ or $\Delta n^2/n^2\ll\Delta E/E$, where L_t is a transverse scale length, and ΔE is the change in the electric field over that length scale. In effect, transversely polarized solutions or TEM modes are an excellent approximation if the transverse variation in the refractive index across the waveguide is much less than the transverse variation in the E field. For guided fields, where most of the field energy is contained within the plasma region, $|\Delta E/E|\sim 1$, while a typical maximum value for the relative index change over the same scale length is $|\Delta n/n|\sim|\Delta N_e/N_e|\sim 10^{-2}$ for the conditions of our experiments [10], where N_e is the electron density. Under these conditions, the polarization term can be neglected and the guided solutions of the wave equation are nearly polarization independent, or TEM modes. We note that for confinement of very high order modes, the transverse index variation must be larger, making the polarization term non-negligible.

Consider an axially invariant plasma waveguide where the plasma index of refraction is given by the Drude model $n^2(\vec{r}_\perp,\omega)=1-\xi+i(\nu/\omega)\xi+4\pi\chi(\vec{r}_\perp,\omega)$, where χ is the total electric susceptibility of the ions and neutrals present in the plasma, ν is the electron-ion collision frequency, $\xi=(\omega_p^2/\omega^2)/(1+\nu^2/\omega^2)$, $\omega_p=\sqrt{4\pi e^2N_e(\vec{r}_\perp)/m_e}$ is the plasma frequency, $N_e(\vec{r}_\perp)$ is the transverse electron density profile, and ω is the laser frequency. We are interested in axially propagating solutions of the form $E(\vec{r}_\perp,z)=u(\vec{r}_\perp)e^{i\beta z}$, where β is the propagation wave number in the plasma waveguide. Neglecting the polarization term in Eq. (1) yields

$$\nabla_\perp^2u(\vec{r}_\perp)+\kappa^2u(\vec{r}_\perp)=0, \tag{2}$$

where $\nabla_\perp^2$ is the transverse Laplacian and κ is the transverse wave number. For the typical conditions of our experiments, $\nu\sim 10^{12}-10^{13}\,\mathrm{s}^{-1}$ for electron-ion and electron-neutral collisions and $\omega\sim 10^{15}\,\mathrm{s}^{-1}$ so that $\nu^2/\omega^2\ll 1$ and the refractive index reduces to $n^2(\vec{r}_\perp,\omega)=1-N_e(\vec{r}_\perp)/N_{cr}$, where $N_{cr}=m_e\omega^2/4\pi e^2$ is the critical density. The transverse wave number is then given by

$$\kappa^2(\vec{r},\omega)=k^2\left(1-\frac{\beta^2}{k^2}-\frac{N_e(\vec{r}_\perp)}{N_{cr}}+4\pi\chi(\vec{r}_\perp,\omega)\right), \tag{3}$$

where $k=\omega/c$ is the vacuum wave number.

The solutions to Eq. (2) can be separated into three categories depending on the behavior of κ^2. For any allowed mode there must be a finite radial region somewhere interior to the channel where $\kappa^2>0$. If $\kappa^2>0$ for all $\vec{r}_\perp$, κ is real everywhere and the solutions are freely propagating *radiation waves*. Solutions with $\kappa^2<0$ everywhere beyond some radial position, say for $|\vec{r}_\perp|>r_m$, are *bound modes*. This is an idealization, however, because in a physical waveguide the electron density drops to zero at some radial position beyond the peak electron density at the shock (see Fig. 1), so that beyond some radius $|\vec{r}_\perp|>r_{\mathrm{out}}$, $\kappa^2>0$ again. Those solutions for physical waveguides which have $\kappa^2<0$ over a finite radial range in the waveguide's electron density barrier region (the shock region) are called *leaky* or *quasibound* modes. There is some confinement of the wave within the interior channel region where $\kappa^2>0$, but tunneling or leaking is allowed to freely propagating waves at $|\vec{r}_\perp|>r_{\mathrm{out}}$. Strictly speaking, there are no bound solutions to plasma waveguides of the type we generate; there are only radiation modes and quasibound modes which are confined to various degrees. In our previous work we have studied the propagation of these quasiguided or leaky modes [14].

Our experimental waveguides have been shown to be cylindrically symmetric [10], so our further analysis below will assume that $u(\vec{r}_\perp)=u(r,\phi)$ in cylindrical coordinates. The solution to Eq. (2) outside the waveguide, where there is no plasma, then gives the field $E(r,\phi,z)=\frac{1}{2}e^{i\beta z}[a_+H_m^{(1)}(\kappa_0r)+a_-H_m^{(1)}(\kappa_0r)]e^{im\phi}$, where $H_m^{(1,2)}$ are mth order Hankel functions of the first and second kind, a_+/a_- is a ratio of complex coefficients depending on the specific plasma structure, $\kappa_0=k(1-\beta^2/k^2+4\pi\chi_0)^{1/2}\equiv k_\perp$ is the transverse wave number outside the plasma-neutral gas boundary (taken to be $r>r_b$), and $\chi_0=\chi(r>r_b)$. Since our experiments are in the low collision frequency regime ($\nu^2/\omega^2\ll 1$) we take $\nu=0$ in the analysis, which gives $|a_+/a_-|=1$. We briefly consider the more general case of $\nu>0$ below and in more detail elsewhere [15].

Well outside the waveguide for $\kappa_0r\gg 1$, the above expression for $E(r,\phi,z)$ becomes (for $m=0$) $E(r,\phi,z)\cong[1/(2\pi\kappa_0r)^{1/2}][a_+e^{-i\pi/4}e^{i\kappa_0r}+a_-e^{i\pi/4}a_-e^{i\kappa_0r}]e^{i\beta z}$, which is a superposition of an inward-directed conical wave $E_{\mathrm{in}}=[a_-e^{i\beta z}/(2\pi\kappa_0r)^{1/2}]e^{-i\kappa_0r}$ and an outward-directed conical wave $E_{\mathrm{out}}=[e^{-i\pi/2}a_+e^{i\beta z}/(2\pi\kappa_0r)^{1/2}]e^{i\kappa_0r}$ which propagate at an angle

$$\gamma=\tan^{-1}\left(\frac{\kappa_0}{\beta}\right), \tag{4}$$

with respect to the z axis.

Any field $u(r,\phi)$ in the plasma waveguide can therefore be viewed as the result of scattering by the plasma structure of an incoming conical wave E_{in} into an outgoing wave E_{out}. A measure of the relative coupling to that field is given by the ratio

$$\eta(k_\perp)=\int_A |u(r,\phi,k_\perp)|^2 dA/|E_{\rm in}|^2 A, \tag{5}$$

where A is the transverse area for $|\vec{r}_\perp|\leq r_{\rm out}$. In general, continuous values of $\kappa_0=k_\perp$ (from variations in β and/or k) are allowed in the solution of Eq. (2), so that η is a continuous function of $k_\perp$. For *radiation modes,* η is of order unity, since the conical wave passes through the plasma with no trapping. However, as the channel expands and a central density depression develops, η can become much greater than unity for narrow distributions of $k_\perp$ centered around certain discrete values $k_{\perp j}$. These are quasi-resonances, which are analogous to cylindrical Fabry-Perot resonances. The buildup of quasiresonant field energy [proportional to the numerator of Eq. (5)] is analogous to the resonant loading of a cylindrical Fabry-Pérot resonator by a wave $E_{\rm in}$, where $E_{\rm out}$ is the leakage wave. For increasing amounts of damping in the shock region of the waveguide [where $\kappa^2(r)<0$], a quasiresonant solution will converge to a bound mode solution and $k_\perp \to k_{\perp j}$.

A description of leaky modes which accounts for such quasiresonant behavior is obtained by considering complex propagation wave numbers $\beta=\beta_r+i\alpha$ as a function of k and $k_\perp$, where α describes attenuation along the guide resulting from tunneling loss of field energy into the field $E_{\rm out}$. The waveguide solution then has the form $u(r,\phi)e^{-\alpha z}e^{i\beta z}$, where the subscript r has been dropped and β now refers to the real part of the propagation wave number. If the jth quasiresonance, say, is sufficiently narrow to have a distinguishable transverse profile $u(r,\phi,k_{\perp j})=u_j(r,\phi)$ associated with it, there is a narrow distribution of β around β_j which can be associated with this mode. Such a quasiresonant mode couples optimally to waves $E_{\rm in}$ and $E_{\rm out}$ that propagate at a mode-specific angle or frequency given by $\gamma(\omega)\approx\tan^{-1}(\kappa_0(\omega)/\beta_j(\omega))$ from Eq. (4). The total field in the waveguide resulting from the distribution in β is described by the Fourier transform pair

$$q_j(z)=\frac{1}{\sqrt{2\pi}}\int_{-\infty}^{\infty}\tilde{q}_j(\beta)e^{i\beta z}d\beta,$$

$$\tilde{q}_j(\beta)=\frac{1}{\sqrt{2\pi}}\int_0^{\infty} q_j(z)e^{-i\beta z}dz, \tag{6}$$

where $q_j(z)$ is defined through $E(r,\phi,z)=u_j(r,\phi)q_j(z)$. Equation (5) can now be reinterpreted as a power spectrum in β near the jth leaky mode,

$$\eta_j(\beta)=|\tilde{q}_j(\beta)|^2=\frac{{A_j}^2/2\pi}{{\alpha_j}^2+(\beta-\beta_j)^2}, \tag{7}$$

with a full width at half maximum of $\Delta\beta=2\alpha_j$, where ${A_j}^2$ is a normalization constant. The power propagating in the waveguide is proportional to $|E|^2\propto e^{-2\alpha z}$, giving a $1/e$ attenuation length of $L_{1/e}=1/\Delta\beta$.

For general channel electron density profiles, the leaky or quasibound modes of a physical waveguide must be found by solving Eq. (2) numerically, and we have developed a code to do so. The code matches, at the plasma-neutral gas boundary, the numerical solution (for $r\leq r_b$) to the solution for $r>r_b$. For the $m=0$ modes, which have their field maximum on-axis, Eq. (5) becomes

$$\eta(k_\perp)=\frac{|u(r=0,k_\perp)|^2}{|u_{np}(r=0,k_\perp)|^2}, \tag{8}$$

where $u(r,k_\perp)$ is the electric field solution to Eq. (2) for a given $k_\perp$, calculated with the plasma present, and $u_{np}(r,k_\perp)=J_0(k_\perp r)$ is the Bessel beam solution for the same $k_\perp$ with no plasma present. For $m\neq 0$, where the solutions do not have on-axis maxima, η must be calculated using the integral formulation of Eq. (5).

An electron density profile which has *bound* analytic solutions, but which is still useful for calculations involving quasibound modes, is the infinite parabolic waveguide with electron density given by $N_e(r)=N_{e0}+N_{cr}(r/a)^2$. Here, a is a curvature parameter and there is no limit on r (so that $\kappa^2<0$ everywhere beyond some radius). The solutions to Eq. (2) for this profile are $u(r,\phi)=a_{pm}e^{-r^2/w_{ch}^2}(2r^2/w_{ch}^2)^{m/2}L_p^m(2r^2/w_{ch}^2)e^{im\phi}$, Laguerre-Gauss functions, where p and m are radial and azimuthal mode indices, a_{pm} is a modal weighting coefficient, and $w_{ch}=a/(\pi r_e N_{cr})^{1/2}$ is the $1/e$ amplitude radius of the lowest order mode. The modal intensity has $(p+1)$ maxima in the radial direction and $2m$ maxima in the azimuthal direction. The discrete propagation wave number associated with these solutions is $\beta_{p,m}^2=k^2-4\pi r_e N_{e0}-(4/w_{ch}^2)(2p+m+1)$ which gives, using Eq. (4),

$$k\tan\gamma\approx\left(4\pi r_e N_{e0}+\frac{4}{w_{ch}^2}(2p+m+1)\right)^{1/2} \tag{9}$$

for small approach angles γ. Equation (9) shows explicitly that side-coupling to a particular (p,m) quasiresonant mode of a given waveguide may be optimized by adjustment of the input angle or wavelength. We note that the solutions for any cylindrically symmetric waveguide can be described by radial and azimuthal mode indices (p,m), and we will use this convention.

Figure 2(a) shows a model profile which illustrates the main qualitative features of the experimental profiles of Fig. 1. For this leaky profile, η from Eq. (8) is shown plotted in Fig. 2(b) versus the normalized wave number $\beta'=\beta/k=\cos\gamma=(1-{k_\perp}^2/k^2)^{1/2}$, for $\lambda=0.57\,\mu$m. The transition between leaky or quasibound modes and radiation modes occurs when the wave is no longer exponentially damped in the electron density barrier [when $\kappa^2(r_m)\geq 0$] and this point is indicated by the arrow at $\beta_{RL}\approx 0.99942k$. For solutions in the radiation zone, $\beta<\beta_{RL}$, it is seen that $\eta\to 1$, indicating that the solutions in the presence of plasma have similar peak amplitude as in the absence of plasma except for small fluctuations due to the phase shift. For $\beta'\to 1, \eta\to 0$ except near the main resonance peak. The solutions which give $\eta\approx 0$ are those for which an incident conical field from outside the guide would experience total reflection from the plasma. The main resonance peak near $\beta'\approx 0.999777$ is identified, by inspection of its corresponding solution u, as the $p=0$, $m=0$ mode. The resonance has a full width at half maximum of $\Delta\beta=2\alpha=0.34\,{\rm cm}^{-1}$, which corresponds to $L_{1/e}=2.9$ cm. For a 1 cm long waveguide, this corresponds to ~30% at-

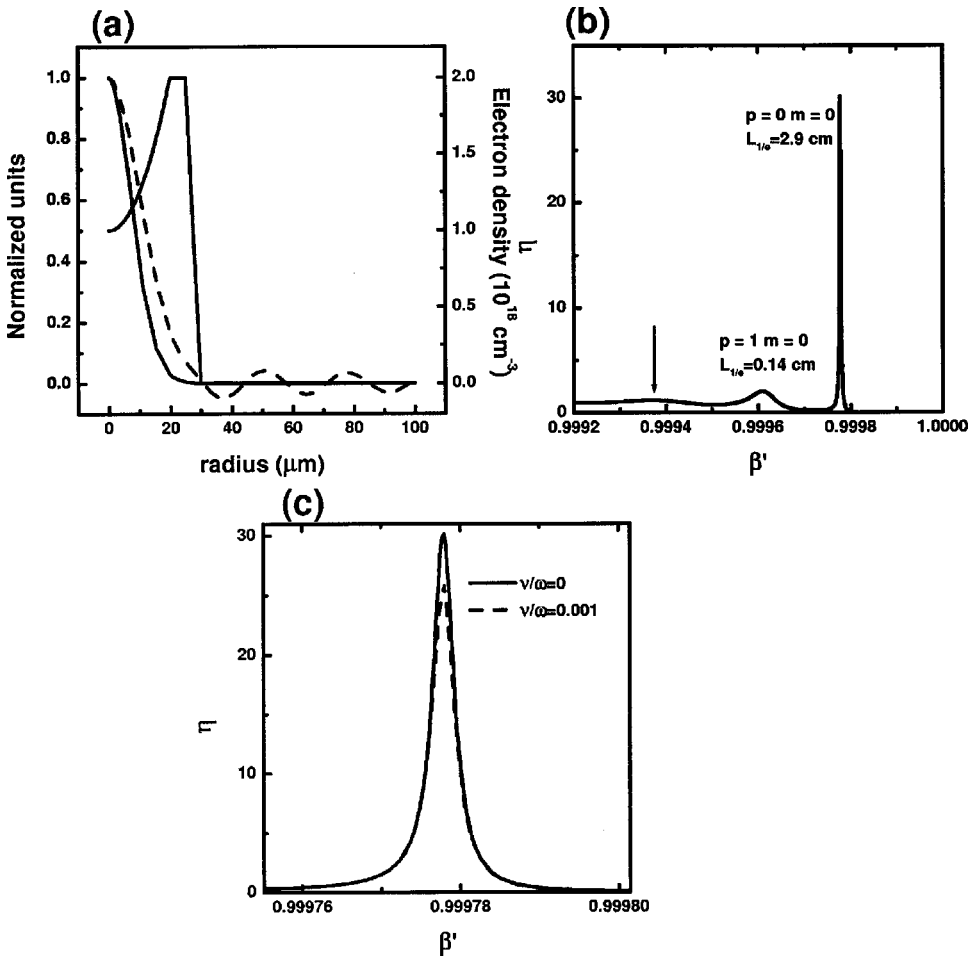

FIG. 2. (a) Leaky parabolic profile $N_e(r)=N_{e0}+\Delta N_e(r^2/r_m^2)$ for $r<r_m$ where $N_{e0}=1\times10^{18}$ cm^{-3}, $\Delta N_e=1\times10^{18}$ cm^{-3}, and $r_m=20\,\mu$m. $N_e=N_e(r=r_m)$ for a radial distance $\Delta r=5\,\mu$m and drops off linearly to zero at $r=r_b=30\,\mu$m. Also shown are the normalized electric field and intensity for the lowest order fundamental mode ($p=0$ $m=0$). (b) Ratio η versus the normalized wave number $\beta'=\beta/k$ for the numerical solutions to the electron density profile of (a) for $\lambda_L=0.57\,\mu$m. The $p=0$ $m=0$ and $p=1$ $m=0$ resonances are identified with their attenuation lengths of 2.9 and 0.14 cm, respectively. (c) Expanded $p=0$ $m=0$ region of (b) with collisions included ($\nu/\omega=0.001$). Collisional absorption results in attenuation length of 2.6 cm.

tenuation. A secondary peak near $\beta'\approx0.9996$ has $\Delta\beta\sim7\,\text{cm}^{-1}$, which gives $L_{1/e}\sim0.14\,$cm. This corresponds to the $p=1$, $m=0$ mode, which would be very strongly attenuated for a 1 cm guiding length. The electric field (dashed curve) and intensity (solid curve) of the $p=0$ $m=0$ mode are overlaid in Fig. 1(a). The electric field shows the Hankel function dependence for $r>r_b$. Also plotted in Fig. 1(b) is η calculated for the case of finite collisions (using the Drude model for $\nu/\omega=0.001$), but this curve nearly overlaps the calculation for zero collisions. Hydrocode simulations [7] show that maximum values of ν/ω are in the range of ~0.001 at the shock peak for the typical plasma waveguides of our experiments. The region in Fig. 2(b) of the $p=0$, $m=0$ resonance is shown expanded in Fig. 2(c), and collisional absorption results in $L_{1/e}=2.6\,$cm, or a reduction in the transmitted energy of $\sim4\%$. This effect is therefore relatively small and $\nu=0$ will be assumed in the subsequent analysis of the experiments.

It is interesting to note that bound mode solutions of Eq. (2) are independent of wavelength [4]. To see this, we rewrite Eq. (2) as $[\nabla_\perp^2-4\pi r_e N_e(\vec{r}_\perp)]u=(\beta^2-k^2)u$, where $r_e=e^2/mc^2=2.82\times10^{-13}\,$cm is the classical electron radius. The left side of this equation is independent of k, so that the eigenvalues (β^2-k^2) and eigenmodes $u(\vec{r}_\perp)$ are wavelength independent. This issue will arise later in Sec. V.

III. END- AND SIDE-COUPLING EFFICIENCY

For a general waveguide, the total transverse field $u(r,\phi)=E_t(r,\phi)$, at a particular position z, can be written as an expansion in the quasiresonant modes, u_{pm}, and the radiation field, E_{rad},

$$E_t(r,\phi)=\sum_{pm} a_{pm}u_{pm}(r,\phi)+E_{\text{rad}}(r,\phi), \tag{10}$$

where $E_{\text{rad}}(r,\phi)$ is considered to contribute negligibly to the total field at that position. Here the coefficients a_{pm} have dimensions of (electric field)$\times$(length) and the functions u_{pm} have dimensions of (length)$^{-1}$. Then $a_{pm}=\int_A E_t u_{pm}^* dA$, where A is the transverse area (for $r<r_b$), and the z-directed power in a given (p,m) mode is given by

$$P_{pm}=\frac{c}{8\pi}|a_{pm}|^2=\frac{c}{8\pi}\left|\int_A E_t u_{pm}^* dA\right|^2. \tag{11}$$

For end illumination of the waveguide (at the plane $z=0$) by a known transverse input field, E_{ti}, the coupling efficiency to a given mode (p,m) is $\varepsilon_{pm}^{\text{end}}=P_{pm}/P_i$, where

$$P_i=(c/8\pi)\int_A |E_{ti}|^2 dA.$$

If side-coupling results in a transverse field E_t in the guide, then the coupling efficiency to a quasibound mode u_{pm} for the case of side injection is

$$\varepsilon_{pm}^{\text{side}}=\left|\int_A E_t u_{pm}^* dA\right|^2 [|E_{\text{in}}|^2 A]^{-1}.$$

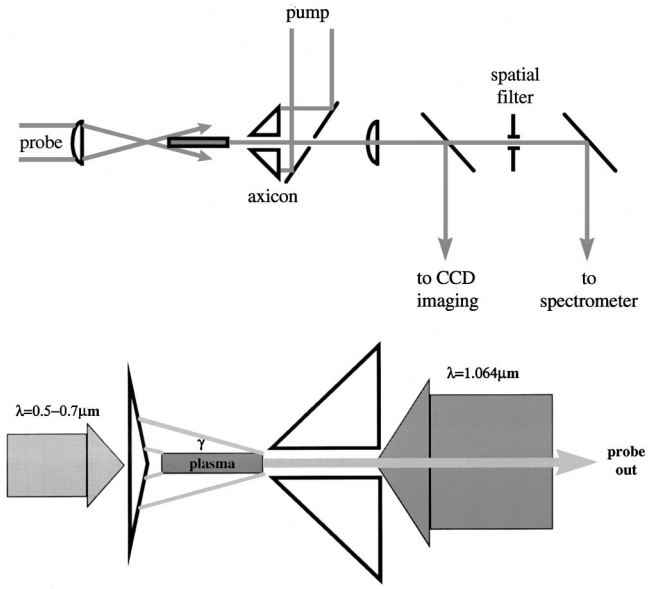

FIG. 3. Experimental setup for (a) end coupling and (b) tunnel coupling.

Note that near a quasiresonance, where u or E_t converges to $a_{pm}u_{pm}$, Eq. (5) reduces to $\eta(k_\perp)=\varepsilon_{pm}^{\text{side}}$. That is, the side-coupling efficiency to a quasibound mode is proportional to the amplitude of the spectral function $\eta(k_\perp)$. For an input wave with a range $\Delta k_\perp$ of $k_\perp$, such as a broad bandwidth pulse, the overall coupling efficiency over that range is proportional to $(1/\Delta k_\perp)\int \eta(k_\perp)dk_\perp$.

IV. EXPERIMENTAL SETUP

The plasma waveguides were formed in an Ar/N_2O backfill gas mixture by pulses (100 ps, 350 mJ, 1064 nm) from a Nd:YAG laser system directed to a ~1 cm line focus by a 35° base angle axicon. The N_2O component field ionizes at $\sim 10^{13}\,\text{W/cm}^2$ which occurs early in the pulse and provides seed electrons for the uniform avalanche breakdown of the argon [10]. Spatially smooth and near-Gaussian synchronous probe pulses (< 1 ps, 1 mJ, 570 nm), generated by a mode-locked R6G dye oscillator/amplifier system [16] were focused into a water cell using $f/30$ optics to produce a continuum in the range $\lambda=500$ to 700 nm [17]. The peak of the spectrum was at 570 nm. The delay between the pump and probe pulses was controlled by a corner cube delay line with continuous delay of −1 to 11 ns.

The experimental setup for end coupling is illustrated in Fig. 3(a). The probe was focused in advance of the plasma waveguide entrance with $f/25$ optics so that it diverged into the waveguide, providing coupling to many quasibound modes. The probe spot size at the waveguide entrance plane was estimated from divergence measurements to be $r_s \sim 100\,\mu$m, which was much larger than the waveguide fundamental spot size w_{ch} for all delays of this experiment. The incident probe intensity of $<10^{12}\,\text{W/cm}^2$ was low enough that probe-induced ionization and heating was negligible. The exit plane of the waveguide was relay-imaged to both a CCD imaging system and a spectrometer (spectral acceptance ~70 nm, resolution ~0.5 nm). Spectral contributions from nonguided sources, such as scattering, were filtered out by a 100 μm spatial filter in the focal plane of a relay lens in the spectrometer arm. Relative confinement of the various quasibound modes was determined by observing the intensity pattern at the channel exit plane. The setup for the tunnel- or side-coupling experiments is shown in Fig. 3(b). The continuum probe beam was recollimated and then directed at $\gamma=4°$ by a coupling axicon to a ~5 cm line focus coincident with the plasma waveguide axis, allowing uniform illumination over the 1 cm length of the plasma waveguide. The chromatic variation of the approach angle γ over the probe's range of wavelengths was ~0.1°. Both the spectrum and the mode image at the exit plane were obtained with the same setup as in the end-coupling experiments.

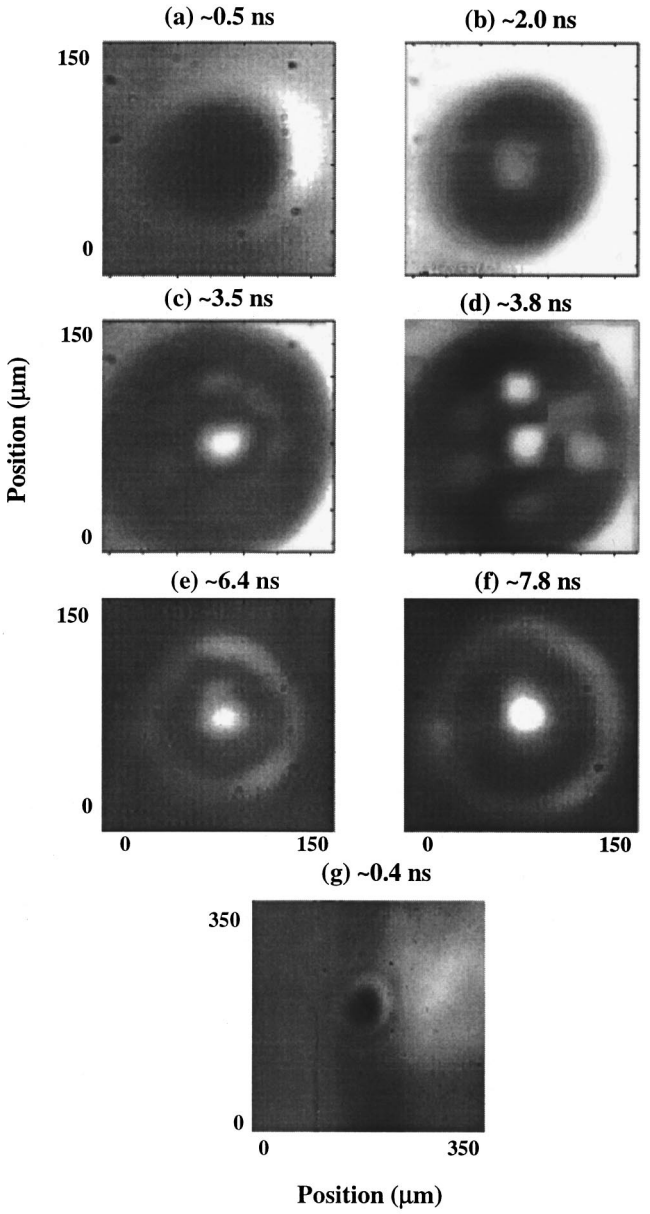

FIG. 4. Single shot exit mode images for probe delays of (a) 0.5 ns, (b) 2.0 ns, (c) 3.5 ns, (d) 3.8 ns, (e) 6.4 ns, and (f) 7.8 ns. (g) Full camera view at a delay of 0.4 ns showing the probe beam position at the waveguide exit.

V. END COUPLING EXPERIMENT: RESULTS AND DISCUSSION

Shown in Fig. 4 is the exit mode image sequence for the 105/20 torr Ar/N_2O gas mixture as the probe delay was increased with respect to the plasma-forming pump pulse. In Fig. 4(a), for a probe delay of 0.5 ns, a dark region centered on the plasma is surrounded by the unguided light of the diverging probe beam, indicating that negligible guided end-coupled light has survived to the end of the guide. The circular dark region of the image is the cross-sectional shadow of the waveguide as seen at its exit. After a delay of ~2 ns, a lowest order $p=0$ $m=0$ guided mode appears at the exit plane [Fig. 4(b)]. The onset of off-axis intensity contributions begins at later delay [Fig. 4(c)], and is followed by a mixture of $m=0$ and $m=3$ modes [Fig. 4(d)]. Since a mode with a radial index p must have $p+1$ rings, we identify the $m=3$ component as having an index of $p=0$. The modes with $m\neq 0$ were distinctly identifiable for only a small range of delay (~0.5 ns) before the onset of azimuthally symmetric exit patterns as in Figs. 4(e) and 4(f), which will be shown below to be a mixture of modes. In general, the appearance of $m\neq 0$ mode structure indicates the presence of azimuthal asymmetry. This asymmetry could be caused by off-center illumination of the end of the waveguide by the probe, a tilt angle between the waveguide and probe beam axes, transverse nonuniformity in the probe beam, or some combination of these. The cause of the asymmetry is shown in Fig. 4(g), which shows a wider view of the exit plane of the waveguide at the early probe delay of ~0.4 ns, where little end coupling has occurred. The probe beam profile (the bright region to the right of the plasma) is uniform and symmetric (the spots are on the neutral density filters used to attenuate the image) but there is an obvious offset between the plasma and the probe. This offset was not due to off-center illumination of the guide end, since optimization of the transverse position of the probe was performed at longer delay such that guided mode patterns were maximized and centered on the waveguide cross section. The offset was therefore attributed to an angular tilt between the guide axis and the probe beam axis, and was estimated to be about ~8 mrads (0.45°). In practice, smaller tilts were difficult to achieve during alignment.

The idealized infinite parabolic profile waveguide discussed in Sec. II can be employed to understand the observed end-coupled intensity profiles. To model the tilted coupling of the probe, we assume end illumination at an abrupt interface between vacuum and an idealized waveguide (oriented along $\hat{z}$), by the Gaussian beam $\vec{E}_i=\hat{e}\exp(-r^2/r_s^2)\exp(i\kappa_\perp x+ik_z z)$ where r_s is the spot size and $\hat{e}$ is the polarization. For small tilt angles θ, $\kappa_\perp\approx k\theta$, $k_z\approx k$, and $\hat{e}\approx\hat{x}$, say. The coupling efficiency $\varepsilon_{pm}^{\text{end}}=P_{pm}/P_i$ into a given (p,m) mode is calculated (see Sec. III) and the optimum coupling angle to a particular $(p=0,m)$ mode can be shown to be [16]

$$\theta_{\text{opt}}=\left[m\frac{2(r_s^2+w_{ch}^2)}{(kr_s w_{ch})^2}\right]^{1/2}. \tag{12}$$

To use this expression to relate the known tilt angle to the observed intensity patterns of Fig. 4 requires knowledge of w_{ch}, the $1/e^2$ intensity radius for the (0, 0) mode. This value cannot be found from the central peak of Fig. 4(d) (which has an intensity HWHM radius of ~12 μm), since that peak contains contributions from the $p=0$, $m=3$ mode as well as from one or more $m=0$ modes. The $p=0$, $m=3$ mode, however, has a well-defined radial position, r_{ring}, where the lobes are located, so that setting $d|u_{0m}|^2/dr|_{r=r_{\text{ring}}}=0$ gives $w_{ch}=\sqrt{2r_{\text{ring}}^2/m}$. The lineout of Fig. 4(d) shown in Fig. 5(a) yields $r_{\text{ring}}\sim 38\,\mu$m which then gives $w_{ch}\sim 31\,\mu$m for $m=3$. For the probe beam wavelength of $\lambda=570$ nm and $r_s\sim 100\,\mu$m, the optimum angle for coupling to the observed $m=3$ mode is ~7.5 mrad (~0.4°), from Eq. (12). This agrees well with the measured tilt angle of 8 mrad from Fig. 4(g).

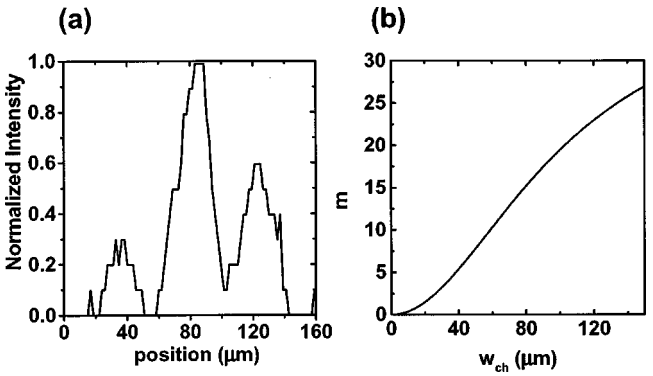

FIG. 5. (a) Lineout of the image of Fig. 4(d). (b) Optimal m versus w_{ch} for an incident angle of 8 mrad.

For a fixed input tilt angle θ, the particular azimuthal mode m which couples most optimally to an evolving waveguide depends on the delay. This mode can be found by rearranging Eq. (12) to give

$$m_{\text{opt}}=\frac{(\theta k w_{ch})^2}{1+(w_{ch}/r_s)^2}, \tag{13}$$

where the channel expansion is represented by increasing values of w_{ch}. Figure 5(b) shows the variation with w_{ch} of the most optimally coupled m mode.

The problem of a finite parabolic waveguide with an electron density profile of $N_e(r)=N_{e0}+N_{cr}(r/a)^2$ for $r<r_m$ and $N_e(r)=N_{em}$ for $r\geq r_m$ has been treated by Durfee *et al.* [14,18]. The requirement on the waveguide depth, $\Delta N_{em}=N_{em}-N_{e0}$, in order for a (p,m) mode to be bound was shown to be

$$\Delta N_{em}>\frac{(2p+m+1)^2}{\pi r_e r_m^2}. \tag{14}$$

For physical waveguides of the type shown in Fig. 1, this criterion is an approximation. It is less applicable to higher order modes which would more strongly radiate out of a real waveguide. It does, however, show the sequence for which modes become more confined through an increase in channel depth and/or radius and it predicts the maximum values of the parameter $\xi=(2p+m+1)$ for modes that are quasibound. Inspection of the channel region of the 1.7 ns profile of Fig. 1 gives $\Delta N_e\sim 2\times 10^{18}\,\text{cm}^3$ and $r_m\sim 25\,\mu$m, which results in $\xi<3.3$ for the confined quasibound modes. Note that the image of Fig. 4(b) (~2.0 ns delay) shows only a single central peak, indicating that any $m\neq 0$ modes either

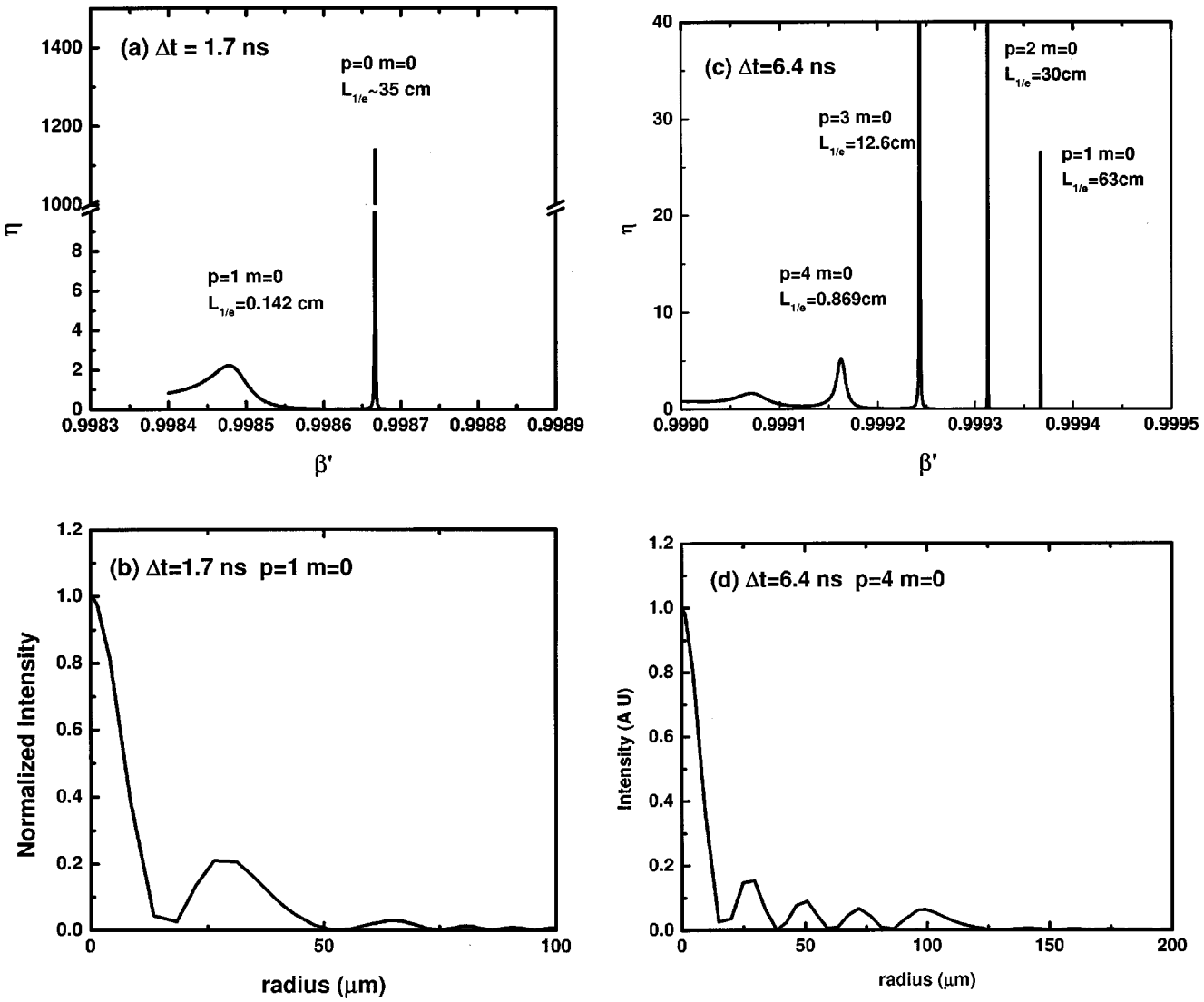

FIG. 6. Numerical solutions of the wave equation showing the ratio η for $m=0$ and electron density profiles at delays of (a) 1.7 ns and (c) 6.4 ns. The radial solutions are shown in (b) for the $p=1$ mode of (a) and shown in (d) for the $p=4$ mode of (c). The $1/e$ intensity attenuation lengths for each resonance are indicated on (a) and (c).

leaked out of the waveguide or were weakly coupled to by the input beam. As the channel became deeper and/or wider, as seen in the profiles of Fig. 1 for delays >3 ns, the channels support higher order quasibound modes. For the delay of 6.4 ns, using $\Delta N_e \sim 2\times 10^{18}\,\mathrm{cm}^3$ and $r_m \sim 65\,\mu\mathrm{m}$, the requirement for quasibound modes is $\xi<8$.

To determine more accurately the modes and their confinement in a real guide, the wave equation must be solved numerically using the experimental density profiles. Shown in Figs. 6(a) and 6(c) is $\eta(k_\perp)$ (see Sec. II), calculated as a function of the normalized wave number $\beta'=\cos\gamma=(1-k_\perp^2/k^2)^{1/2}$ and using $\lambda=570\,\mathrm{nm}$, for the 1.7 ns and 6.4 ns electron density profiles of Fig. 1. As discussed in Sec. II, the peaks in these plots correspond to the quasiresonant modes, and the peak widths are related to the spatial leak rate of these modes. The $1/e$ intensity attenuation length along the guide axis, $L_{1/e}=(\Delta\beta)^{-1}$, of each mode (p,m) is indicated on the plots. Figures 6(b) and 6(d) show the intensity profiles for the $p=1$ mode of Fig. 6(a) and the $p=4$ mode of Fig. 6(c). The peak width of the $p=1$ resonance of Fig. 6(a) $(\Delta\beta\sim 7\,\mathrm{cm}^{-1}, L_{1/e}\sim 0.142\,\mathrm{cm})$ indicates that this mode and modes of higher order $(\xi>3)$ would not be observed at the exit of a 1 cm long guide. The $p=1$ and higher order modes radiate out of the waveguide at angles with respect to the waveguide axis of $\gamma_j=\cos^{-1}(\beta_j/k)$, the smallest of which is $\sim 3.2°$ for the $p=1$ $m=0$ mode. By comparison, the $p=0$ $m=0$ quasiresonance has $L_{1/e}\sim 35\,\mathrm{cm}$ and would therefore experience little tunneling loss. Leak rates for the $p=0$, $m=1$, and the $p=0$, $m=2$ modes were estimated from similar resonance plots to be $L_{1/e}\sim 10\,\mathrm{cm}$ and 1 cm, respectively. The good confinement of these modes is consistent with our earlier estimation of $\xi<3.3$. Figure 6(c) shows that many quasibound modes are supported by the channel at 6.4 ns delay. The plot shows that all modes for $\xi=2p+m+1<9$ are well guided for a 1 cm long waveguide, and this is in reasonable agreement with the value of ξ obtained above. Note that the code cannot resolve numerically extremely narrow resonances, and therefore in Fig. 6(c) the $p=0$ resonance is missed by the calculation and the $p=1$ resonance is shown with artificially reduced amplitude.

The increase in confinement with delay is shown in Fig. 7 where the measured relative energy throughput of the guide

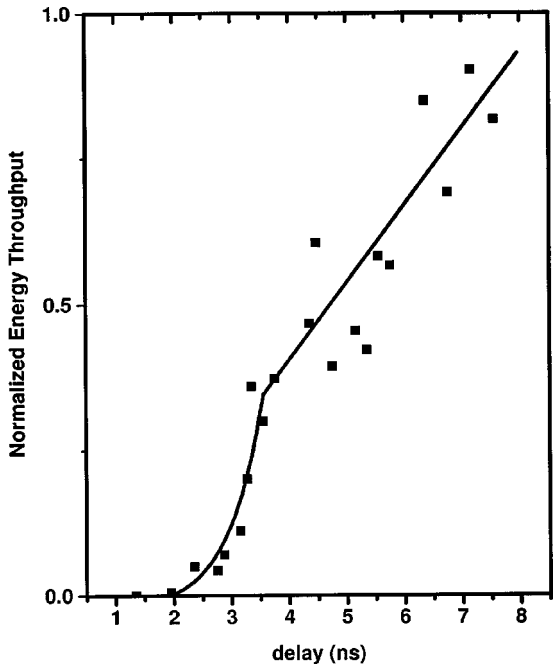

FIG. 7. Normalized energy throughput versus probe delay: each data point represents the integrated guided intensity of a single shot exit mode profile. The exponential fit for delays <3.5 ns and the linear fit for delays >3.5 ns are included as a guide to the eye.

is plotted versus probe delay. The throughput was measured by integrating the guided portion of the single shot exit plane images, which was identified as the intensity within the plasma region [see Fig. 4(g)]. Note the rapid increase in guided energy beginning at a delay of ~2.5 ns.

In addition to considering confinement of particular modes, we must also determine the relative efficiency of coupling to them. Together, this information can be used to understand the experimentally observed waveguide exit profiles. Using Eq. (11), and a tilt angle of 8 mrad, we plot in Fig. 8(a) the end-coupling efficiency $\varepsilon_{pm}^{\mathrm{end}}$ versus m to ($p=0,m$) modes of the 1.7 ns profile ($w_{ch}\sim 12\ \mu$m) and the 6.4 ns profile ($w_{ch}\sim 50\ \mu$m) of Fig. 1. For the 1.7 ns profile, we showed above that the $p=1$, $m=0$ mode and higher p modes would radiate away and not be observed. The image of Fig. 4(b), at a delay of ~2.0 ns, shows a low intensity central spot with little evidence of any off-axis rings or lobes. The rapidly decreasing coupling efficiency with increasing m in Fig. 8(a) suggests that the $p=0$, $m=0$ mode should dominate the exit mode pattern, and this is in good agreement with Fig. 4(b). For the 6.4 ns delay [Fig. 4(e)], it is expected from the $L_{1/e}$ calculations above that no modes of order higher than $p=4$ $m=0$ should contribute. For (p,m) modes of decreasing ξ, the confinement was seen to increase from $L_{1/e}\sim 1$ cm for $\xi=9$, to $L_{1/e}\sim 12$ cm for $\xi=7$, the latter giving attenuation along a 1 cm guide of ~8%. We therefore consider modes with $\xi\leqslant 7$. The central intensity half-maximum radius of ~15 μm in Fig. 4(e) is explained by the contributions of higher order p modes, as illustrated in Fig. 8(b), which shows the composite intensity profile $I=|\Sigma_{p=0}^{3}u_{p0}(r)/A_{p0}|^2$ of the $m=0$ $p=0$, 1, 2, and 3 modes (which are assumed to be in phase and normalized to unity), for $w_{ch}=50\ \mu$m. For these $p>0$ modes, therefore, a central peak dominates the intensity profile, with very weak contributions off axis. To explain the ring in Fig. 4(e), $m>0$ modes must then be considered. Using the coupling efficiencies of Fig. 8(a) for the 6.4 ns profile as weighting factors, the total $p=0$, $m>0$ field is calculated as the sum of the modes for $m\leqslant 6$ (due to our $\xi\leqslant 7$ requirement). The resulting intensity profile $I=|\Sigma_{m=1}^{6}\sqrt{P_{0m}/P_i}u_{0m}(r)/A_{0m}|^2$ is shown in Fig. 8(c), where $\varepsilon_{0m}^{\mathrm{end}}=P_{0m}/P_i$ is the intensity coupling efficiency for each mode. The profile from Fig. 8(b) has been replotted in Fig. 8(c) (dotted curve) to illustrate both $m=0$ and $m>0$ contributions at the exit plane. The dominant single ring in Fig. 4(e) is thus explained from the dependence of the coupling efficiencies on m, shown in Fig. 8(a) to peak at $m=6$ and drop off for higher and lower m. The asymmetry introduced by the tilt angle of 8 mrad therefore favors $m\sim 6$ for this electron density profile. The guide, however, exhibits strong leakage for $\xi>7$, which limits the $p=1$ and $p=2$ contributions to have $m\leqslant 4$ and $m\leqslant 2$, respectively. The combination of the leakage and asymmetry therefore result in the selection of the $p=0,m\sim 6$ modes which together produce a smooth ring (as the $2m$ lobes merge). The mode pattern of Fig. 4(e) is therefore explained as the result of numerous $m=0$ modes contributing to the central peak and the $p=0$ $m\sim 6$ modes contributing to form a smooth off-axis intensity ring.

For all delays after the appearance of the $m=3$ mode, the waveguide exit intensity profile was characterized by a central peak surrounded by a single dominant ring of approximate azimuthal symmetry, whose radius increased with delay. As shown above, longer delays allow increased confinement of $p>0$ modes, adding dominantly to the central maximum. Also, w_{ch} increases with delay, leading to an increase in the optimal m for a fixed tilt angle [see Eq. (13) and Fig. 5(b)]. The radial position of the peak of the ring (which becomes increasingly smooth) then increases according to $r_{\mathrm{ring}}=\sqrt{m w_{ch}^2/2}$.

The spectrum measured for the exit modes was found to be smooth and unchanging as the probe delay was increased. Figures 9(a)–9(c) show the sequence of spectra for probe delays of 2.5 ns, 3.5 ns, and 8.0 ns taken as 10 shot averages to eliminate shot to shot amplitude variations. These variations were due to laser energy fluctuations. Figure 9(d) shows a single shot spectrum at a delay of 5.8 ns. At all delays for end coupling at these intensities, there was no change in the spectrum due to guiding. This is consistent with the discussion of Sec. II: the quasibound modes which survive to the end of the guide are well-bound, and in the limit of strong binding, we showed that transverse mode structure was independent of wavelength. Therefore, for all the well-bound end-coupled modes shown in Fig. 4 the spectrum remains the same. This is in direct contrast to the spectral effects of side or tunnel coupling described in the next section.

VI. SIDE-COUPLING EXPERIMENT: RESULTS AND DISCUSSION

Shown in Fig. 10 is a sequence of spectrally integrated end mode images for a 130 torr Ar/20 torr N_2O gas mixture as the side-coupled probe delay (with respect to the channel creation pulse) was increased. During the initial stages of channel formation, coupling occurred to the lowest order

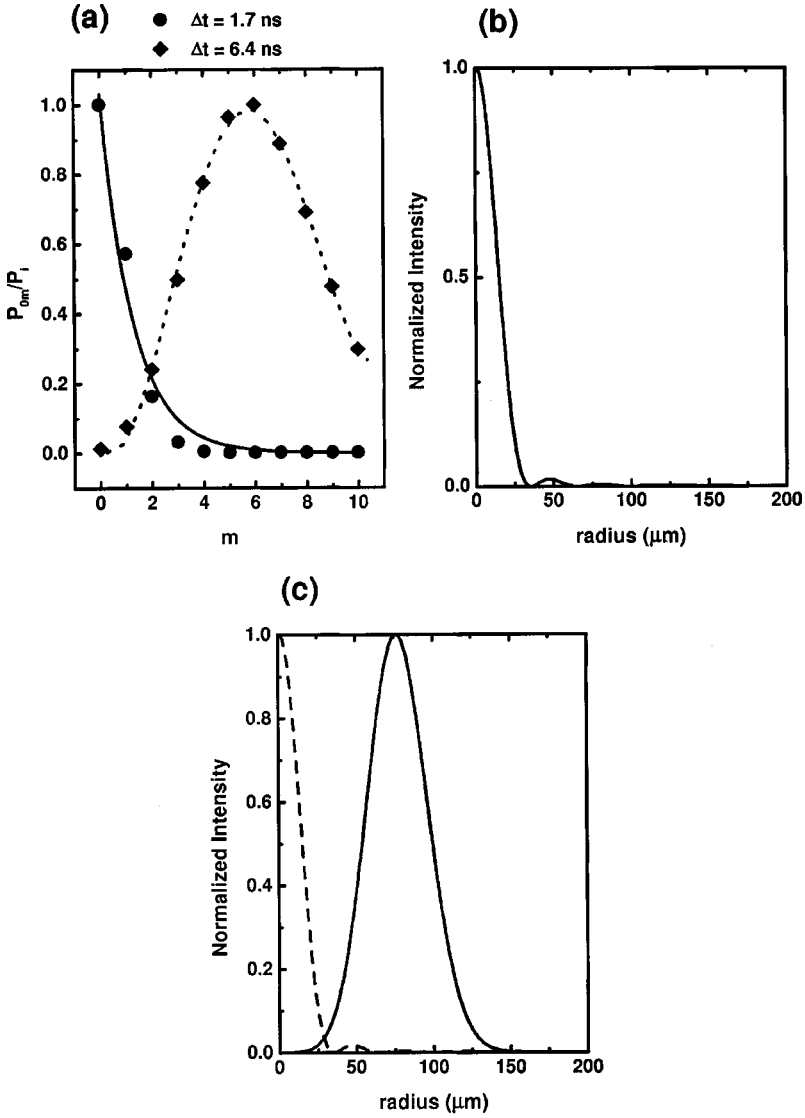

FIG. 8. (a) Calculated modal coupling efficiency (for $p=0$) versus azimuthal mode index m for an incident angle of 8 mrad for the $\Delta t = 1.7$ ns profile and $\Delta t = 6.4$ ns. (b) Intensity profile of the sum of wave equation solutions $p=0$, 1, 2, and 3 ($m=0$) for $w_{ch}=50\ \mu$m. (c) Intensity profile of the sum of wave equation solutions $p=0$ $m\leqslant 6$ (solid curve) and $p\leqslant 3$ $m=0$ [dashed curve same as in (b)].

($p=0,m=0$) mode [Fig. 10(a) at 0.5 ns]. By comparison, note that Fig. 4(a), for the same delay, shows that negligible end-coupled light has survived to the end of the guide. The on-axis intensity of this mode increased rapidly and then decreased (see Fig. 13 and related discussion below) before $p=0,m=1$ and higher m modes appeared by 0.6 ns [Fig. 10(b) and 10(c)]. Note in Fig. 10(c) that the azimuthal lobes have merged to form a fairly smooth ring. The basis for the identification of these as $p=0,m>0$ modes is the fact that $p\geqslant 1$ modes have $p+1$ rings and $m=0$ modes have maxima on-axis, neither of which appear here. At longer delay, 0.9 ns in Fig. 10(d), more azimuthal lobes are present, with apparent merging into a ring. When the probe beam bandwidth was reduced to $\sim$2 nm at the same delay, a specific azimuthal mode ($m=2$) with clearly identifiable lobes appeared [Fig. 10(e)]. As in the case of end coupling, the presence of lobes ($m>0$) indicates the breaking of azimuthal symmetry due to small residual tilt between the waveguide and coupling beam axes or transverse asymmetry in the coupling beam profile. It was verified that a slight tilt of the coupling beam changed the orientation and number of lobes, as well as the delay time for their onset. Although the coupling beam was quite azimuthally symmetric, it was also found that by blocking, say, the left or right side of the beam, lobe structures were oriented left-right. At even longer delay (2.2 ns), Figs. 10(f) and 10(g) show how [as in Fig. 10(d) and 10(e)] reducing the bandwidth reduces a ringlike structure of merged lobes to a specific azimuthal mode. These results suggest that spectral components of the continuum probe were resonant with several modes and that the ringlike exit patterns are of spectrally integrated mixtures of these modes.

Equation (4) suggests that at fixed approach angle γ (here 4°), the process of side injection will result in some frequency selection, since the position in $k_\perp$ space of the quasiresonances will now depend on k. Figure 11 shows spectra measured at the waveguide exit from side-coupled continuum probe pulses centered at $\lambda\sim 570$ nm as a function of early delay for the same waveguide conditions as in Fig. 10. At 500 ps [Fig. 11(a)], the onset of side coupling is seen in a relatively narrow spectral region. The broader and relatively smooth input spectrum is shown overlaid for comparison. As the delay was increased to 530 ps [Fig. 11(b)], coupling increased, more peaks appeared, and the overall guided spectrum was broadened. This process continued in Fig. 11(c), at 550 ps delay. At delays beyond $\sim$1 ns, coupling in this wavelength region decreases. We observed generally that the bluer portion of the probe spectrum was better coupled for higher fill pressures and early delays [consistent with higher

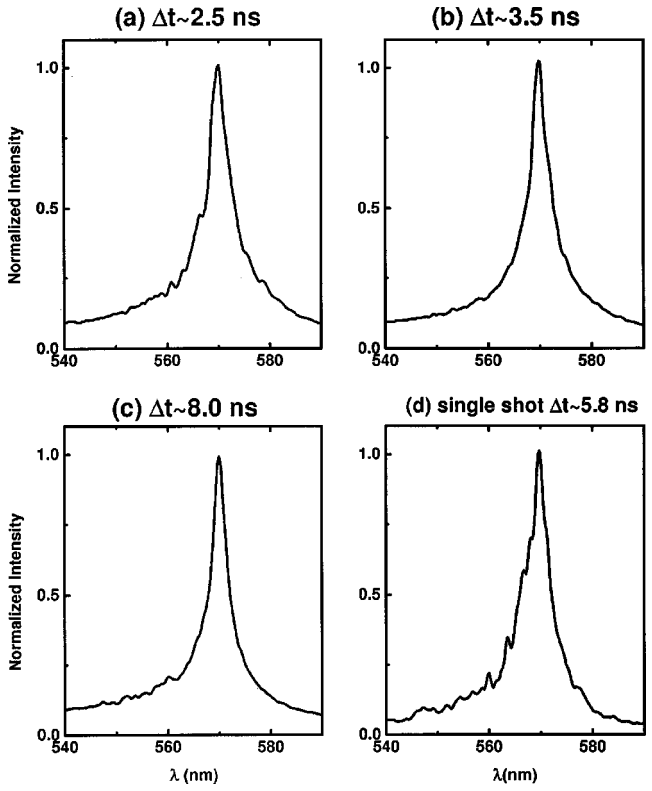

FIG. 9. Spectra of guided probe pulse for delays of (a) 2.5 ns, (b) 3.5 ns, and (c) 8.0 ns taken as 10 shot averages. The single shot spectrum for 5.8 ns delay, shown in (d), is representative of the shot-to-shot fluctuations.

values of N_{e0} and smaller values of w_{ch}, as predicted by Eq. (9)]. At longer delays or lower initial fill pressures, better coupling occurred to redder wavelengths, as is illustrated by the spectrum centered at ~700 nm in Fig. 11(d). No distinct peaks for the full range of probe wavelengths were seen at any delay for pressures lower than 70 torr (50 torr Ar/20 torr N_2O). This is explained by considering the minimum requirement for the confinement of a quasibound mode (see Sec. II), $\kappa_s^2 = k^2 - \beta^2 - 4\pi r_e N_{es} < 0$ (or the equivalent expressions $\lambda > \lambda_{qb} = \sqrt{\pi / r_e N_{es}} \sin\gamma$ or $N_{es} > N_{cr} \sin^2\gamma$), where κ_s is the transverse wave number at the peak of the electron density barrier at the shock (where $N_e = N_{es}$). Using $\gamma = 4°$ for our probe beam axicon and $N_{cr} \sim 2 \times 10^{21}\,\mathrm{cm}^{-3}$ at the longest probe wavelength of ~730 nm, quasibound mode confinement requires $N_{es} > 10^{19}\,\mathrm{cm}^{-3}$, which was achievable only at pressures greater than 70 torr. In effect, fill pressures $\leqslant$70 torr did not support quasibound modes for the probe spectral region and incidence angle of this experiment. In Fig. 12, the waveguide spectral function $\eta(k_\perp)$ is plotted (for $m = 0$) as a function of wavelength (at fixed $\gamma = 4°$), where $k = k_\perp / \sin\gamma$, for the measured 900 ps electron density profile shown in the inset (for the conditions of Fig. 10). As discussed in Sec. III, the amplitude of η is proportional to the coupling efficiency of the corresponding quasibound mode. In the shorter wavelength range, where $\eta \sim 1$, the conical input is mainly transmitted through the plasma with little coupling to quasibound modes. Values of $\eta \sim 0$, on the long wavelength side of the main resonance peak, correspond to a total reflection of the input wave from the outside of the waveguide. The additional effect of azimuthal coupling asymmetry ($m > 0$) can be estimated using the expression for parabolic waveguides, Eq. (9), which gives $\Delta\lambda/\lambda = \Delta\omega/\omega = \lambda^2 / 2\pi^2 w_{ch}^2 \tan^2\gamma$ for adjacent ($\Delta m = \pm 1$) azimuthal modes.

These mode positions are overlaid on the plot for $\gamma = 4°$ and $w_{ch} \sim 20\,\mu$m [obtained by solving Eq. (2) for the measured profile]. The peak spacings of ~4 nm, denoted by the dashed lines, are in good agreement with the spectral peak separations in Fig. 11. The onset of quasibound modes for this density profile, λ_{qb}, is indicated by the arrow on the λ axis.

VII. COMPARISON OF END-COUPLING AND SIDE-COUPLING EXPERIMENTS

The steady state analysis based on Eq. (2) presumes that the peak widths $\Delta\beta$ in the spectral function η are controlled by the balance between the inverse processes of axial growth of the side-coupled field and losses from radiative leakage of the quasibound mode. We can extract a spatial leak rate from Fig. 11 by noting that at the jth quasibound mode the leak

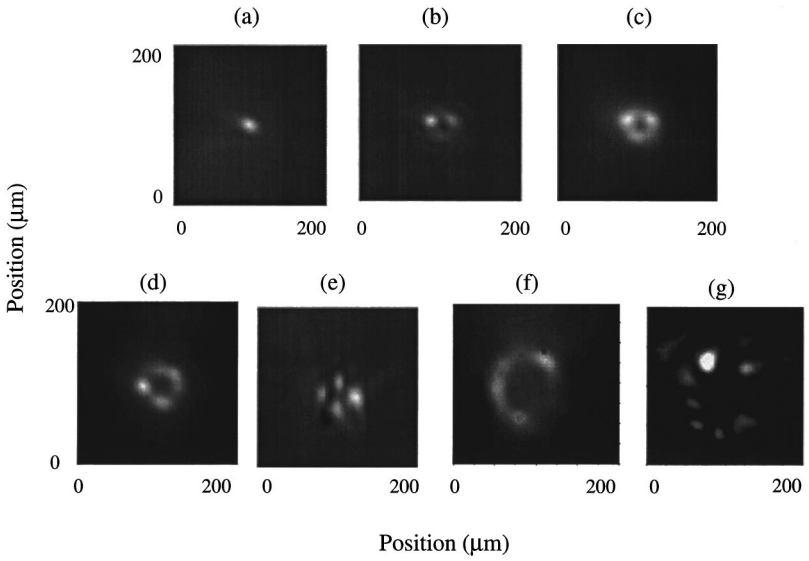

FIG. 10. Spectrally integrated channel exit images of side coupled continuum probe for pump-probe delays (a) 0.5 ns, (b) 0.56 ns, (c) 0.59 ns, (d) 0.9 ns, (e) reduced bandwidth (~2 nm) probe, delay ~0.9 ns (130/20 torr Ar/N_2O gas fill), (f) continuum probe with delay of 2.2 ns, (g) reduced bandwidth probe, delay ~2.2 ns (80/20 torr Ar/N_2O gas fill).

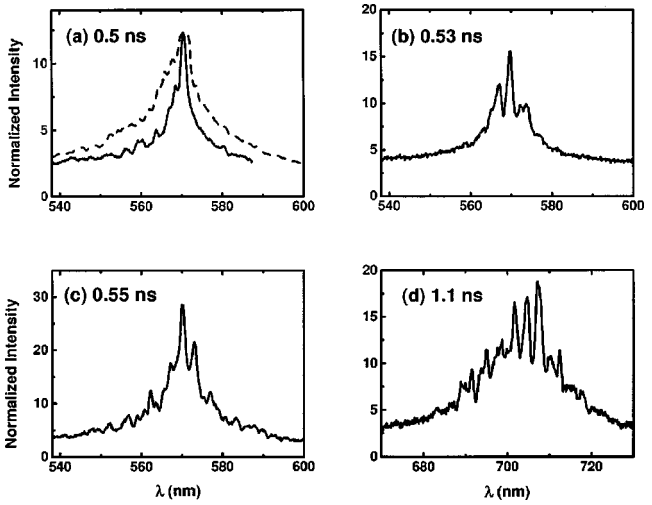

FIG. 11. Spectrum of side-coupled probe for indicated pump-probe delays. (a)–(c) 130/20 torr Ar/N_2O, (d) lower pressure fill: 80/20 torr Ar/N_2O. The probe input spectrum near 570 nm (shown normalized for comparison) is the dashed line in (a).

rate is $\alpha_j=(\Delta\beta)^{-1}\approx\Delta\omega_j(d\beta/d\omega)_{\omega=\omega_j}=(\Delta\omega_j/c)\cos\gamma$. The spectral peak widths $\Delta\lambda$ of ~1.5–2 nm give α^{-1} ~150 μm, which is much less than the waveguide length. This indicates that the steady state analysis is justified and also implies that end-coupled light at these delays would have been strongly attenuated. This is confirmed in the plot [Fig. 13(a)] of spectrally integrated energy throughput, comparing side and end coupling, which shows that the early delay range of best side coupling corresponds to negligible end coupling throughput. End-coupled throughput begins to increase at longer delays, as shown in Figs. 13(a) and 13(d), where leakage and therefore side coupling, its inverse, decreases. In effect, in terms of the theory of Sec. II, side-coupling provides a continuous input field $E_{\rm in}$ along the full length of the guide, which compensates for the leaking wave $E_{\rm out}$ at early delays. For end-coupled light, however, $E_{\rm in}=0$, so that the weakly bound waveguide modes at early delay attenuate rapidly and are not observed at the exit. Side coupling therefore allows the probing of mode structure associated with the earliest times in the waveguide development, and this early time mode selectivity can be seen in the first 1.5 ns of side-coupling delay shown expanded in Fig. 13(b). The rise of the first sharp peak occurs as side-coupling rapidly increases to the $p=0,m=0$ mode [see Fig. 10(a)]. The decrease to a minimum after ~50 ps for these conditions occurs at the transition to the $p=0,m=1$ mode [see Fig. 10(b)]. The second, broader peak then increases as additional azimuthal lobes accumulate. The third, broad peak beginning around 1.25 ns in Figs. 13(a) and 13(b), arises as the red portion of the spectrum couples more efficiently as N_{e0} decreases at longer delay (see the electron density profiles of Fig. 1).

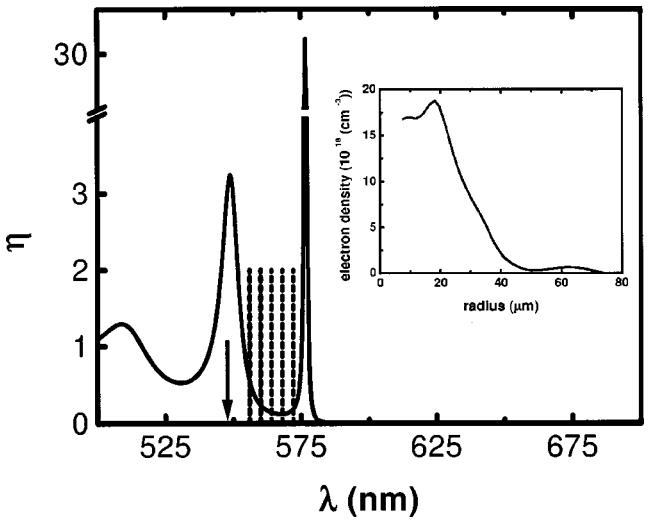

FIG. 12. Calculation of relative coupling efficiency versus wavelength for measured electron density profile (inset), 900 ps delay, 130/20 Ar/N_2O. Dotted vertical lines: positions of $m\neq0$ modes. Arrow: location of λ_{qb}.

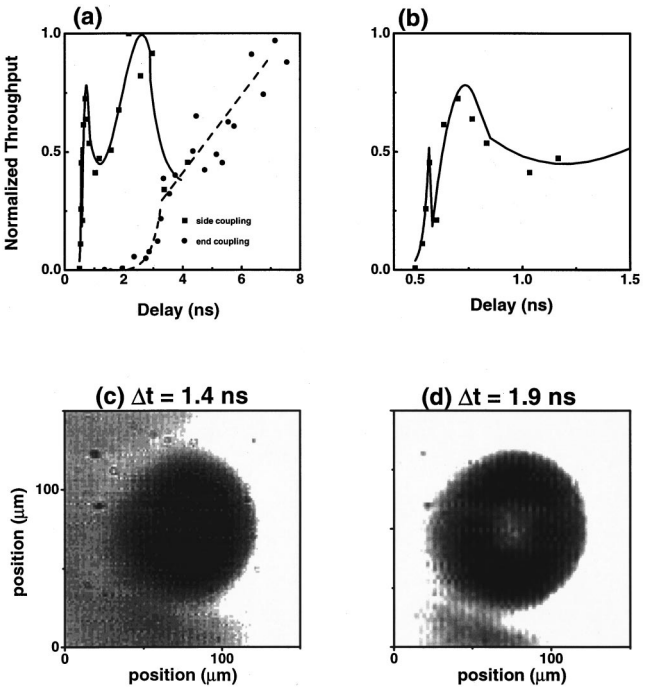

FIG. 13. (a) Spectrally integrated energy throughput versus delay for side and end coupling (curves are separately normalized); (b) expanded time scale for (a); (c) and (d) channel exit images for end coupling at indicated delays (105/20 torr Ar/N_2O).

Finally, the spectral signature of well-bound vs very leaky modes (or end coupling vs side coupling) is that the more strongly bound modes, which are accessed through end-coupling at longer delays, were seen to have spectra independent of mode structure, while side coupling to weakly bound leaky modes is wavelength selective.

VIII. CONCLUSIONS

The quasibound modes of a plasma waveguide were probed using side- and end-coupling geometries in order to study two temporal regimes: early-time plasma channel development, characterized by leaky optical confinement, and later channel hydrodynamic expansion characterized by stronger confinement. Both the intensity pattern and the spectrum of the guided light were measured at the channel exit. For end coupling, the modal intensity observed at the

exit was determined by two factors: the input coupling efficiency, and the axial leak rates of the various modes to which coupling was achieved. The small angle between the input beam axis and the waveguide axis was found to be important in determining the measured $m>0$ mode structure. The spectrum of broadband end-coupled probe pulses was found to be unaffected by the guiding process, mainly because those modes which survived to the waveguide exit were well bound, and for strongly-bound fields, the transverse mode profiles are wavelength independent. By contrast, side coupling to the quasibound modes of the plasma waveguide was seen to be highly mode and frequency selective. Both end-coupled and tunnel-coupled exit intensity profiles and spectra were successfully explained using calculations based on the experimentally measured electron density profiles.

ACKNOWLEDGMENTS

This work was supported by the National Science Foundation (Grant No. PHY-9515509) and the DOE (Contract No. DEF G0297 ER 41039).

[1] C. J. Joshi and P. B. Corkum, Phys. Today **48**, 36 (1995).
[2] K. Krushelnick, A. Ting, C. I. Moore, and H. R. Burris, Phys. Rev. E **57**, 2475 (1998); C. E. Clayton, K.-C. Tzeng, D. Gordon, P. Muggli, W. B. Mori, C. Joshi, V. Malka, Z. Najmudin, A. Modena, D. Neely, and A. E. Dangor, Phys. Rev. Lett. **81**, 100 (1998).
[3] A. Rundquist, C. G. Durfee III, C. Zenghu, C. Herne, S. Backus, M. M. Murnane, and H. C. Kapteyn, Science **280**, 1412 (1998).
[4] H. M. Milchberg, C. G. Durfee III, and T. J. McIlrath, Phys. Rev. Lett. **75**, 2494 (1995).
[5] J. J. Rocca, V. N. Shlyaptsev, F. G. Tomasel, O. D. Cortazer, D. Harshorn, and J. L. A. Chilla, Phys. Rev. Lett. **73**, 2192 (1994); H. M. Milchberg, C. G. Durfee III, and J. Lynch, J. Opt. Soc. Am. B **12**, 731 (1995).
[6] T. Tajima and J. M. Dawson, Phys. Rev. Lett. **43**, 267 (1979); P. Sprangle, E. Esarey, A. Ting, and G. Joyce, Appl. Phys. Lett. **53**, 2146 (1988).
[7] C. G. Durfee III and H. M. Milchberg, Phys. Rev. Lett. **71**, 2409 (1993).
[8] Y. Ehrlich, C. Cohen, and A. Zigler, Phys. Rev. Lett. **77**, 4186 (1996).
[9] A. B. Borisov *et al.*, Phys. Rev. Lett. **68**, 2309 (1992); P. Monot *et al.*, *ibid.* **74**, 2953 (1995); K. Krushelnick *et al.*, *ibid.* **78**, 4047 (1997); R. Wagner *et al.*, *ibid.* **78**, 3125 (1997); J. Fuchs *et al.*, *ibid.* **80**, 1658 (1998).
[10] T. R. Clark and H. M. Milchberg, Phys. Rev. Lett. **78**, 2373 (1997).
[11] H. M. Milchberg, T. R. Clark, C. G. Durfee III, and T. M. Antonsen, Phys. Plasmas **3**, 2149 (1996).
[12] S. P. Nikitin, I. Alexeev, J. Fan, and H. M. Milchberg, Phys. Rev. E **59**, R3839 (1999).
[13] T. R. Clark and H. M. Milchberg, Phys. Rev. Lett. **81**, 357 (1998).
[14] C. G. Durfee III, J. Lynch, and H. M. Milchberg, Opt. Lett. **19**, 1937 (1994); C. G. Durfee III, J. Lynch, and H. M. Milchberg, Phys. Rev. E **51**, 2368 (1995).
[15] J. Fan, E. Parra, and H. M. Milchberg, Bull. Am. Phys. Soc. Plasma Phys. **44**, 254 (1999).
[16] T. R. Clark, Ph.D. dissertation, University of Maryland, 1998.
[17] R. L. Fork, C. V. Shank, C. Hirlimann, R. Yen, and W. J. Tomlinson, Opt. Lett. **8**, 1 (1983).
[18] C. G. Durfee III, T. R. Clark, and H. M. Milchberg, J. Opt. Soc. Am. B **13**, 59 (1996).